Contrast-Enhanced Composites via Hafnium Oxide Nanocrystal-Coated Carbon Fibers

Eline Goossens,[†,‡] John De Vos,[†] Matthieu N. Boone,[¶] Isabel Van Driessche,[†] Jonathan De Roo,[‡] Wim Van Paepegem,[§] and Klaartje De Buysser[*,†]

†*Department of Chemistry, Ghent University, 9000 Ghent, Belgium*

‡*Department of Chemistry, University of Basel, 4058 Basel, Switzerland*

¶*Center for X-ray Tomography, Ghent University, 9000 Ghent, Belgium*

§*Department of Materials, Textiles and Chemical Engineering, Ghent University, 9052 Zwijnaarde, Belgium*

E-mail: Klaartje.DeBuysser@UGent.be

Abstract

Carbon fiber reinforced polymers (CFRP) are of utmost importance in high-performance structural applications such as aerospace, automotive and wind energy. Modelling of their behaviour starts from accurate and straightforward geometry reconstruction, which is currently unfeasable due to a lack of Computed Tomography (CT) contrast. We explore the potential of hafnium oxide nanocrystals (HfO_2 NCs) as CT contrast agents by coating the NCs on the carbon fiber surface. The enhanced CT contrast makes for a stark contrast difference between pure polymer matrix to carbon fiber fabric, allowing for automatic segmentation. To ensure a dense and well-dispersed coating, solution dipcoating and airbrushing were used. Both techniques yield drastic CT contrast improvements over a range of HfO_2 NC concentrations on the interface between different tows. Furthermore, we explore the potential of an NC-airbrushed squared

https://doi.org/10.26434/chemrxiv-2024-cl440 **ORCID:** https://orcid.org/0000-0002-4653-7570 Content not peer-reviewed by ChemRxiv. **License:** CC BY-NC-ND 4.0

pattern of NCs as internal trackers in digital volume correlation (DVC), expanding the possible visualization and measurement techniques to understand CFRP behavior.

Introduction

Fiber reinforced polymers (FRPs) realize excellent strength-to-weight ratio's by combining a light polymer matrix with strong reinforcing fibers. This unique combination makes them paramount to weight-critical structural applications such as wind energy,[1] aerospace,[2] automotive[3] and more.[4,5] The transfer of stress from the relatively weak polymer to the fibers is mediated by the fiber/matrix interface, which is therefore key to optimizing the mechanical properties.[6,7] Strong fiber-to-matrix interactions are necessary, *i.e.* the interfacial adhesion energy should exceed the polymer cohesion energy.[8] The vast majority of carbon fibers are polyacrylonitrile (PAN) based.[6] Carbonization and graphitization steps during manufacturing create a hydrophobic and inert surface.[8,9] Fiber sizing is a thin, homogeneous coating of polymer. It is often applied by the manufacturer to the carbon fiber surface to improve the adhesion and to protect the brittle fibers.[10] Several surface modifications have been used to further improve the fiber/matrix interface either by increasing the surface roughness or the surface reactivity.[9] Coating of the fibers with nanoparticles (NPs) has shown to increase surface roughness, which improves the interfacial strength, together with other parameters such as tensile strength and tribological properties.[7,11–13] Carbon nanotubes (CNTs) are also popular nanomaterials to coat the fiber surface,[14–16] though it is challenging to obtain a homogeneous dispersion on the surface.[7] Solution dipcoating is often used to disperse a variety of CNTs and other NPs on the fiber surface.[17,18] While less explored, airbrushing has also been applied to coat fibers with CNTs[19,20] and NPs.[21] Airbrushing is typically preferred for high coating concentrations.

While NP-coated fibers for improved mechanical properties in FRPs have gained interest, there are little to no studies using NPs on the fiber surface for visualization. Micro-Computed

https://doi.org/10.26434/chemrxiv-2024-cl440 **ORCID:** https://orcid.org/0000-0002-4653-7570 Content not peer-reviewed by ChemRxiv. **License:** CC BY-NC-ND 4.0

Tomography (micro-CT) data provides high-resolution three-dimensional (3D) data of the sample and has therefore developed as an important input or validation for composite behavior models.[22] Selective visualization of the interface between tows on would simplify geometry extraction, but the lack of CT contrast between the carbon fibers and the polymer matrix makes this extremely challenging. Deep learning algorithms are increasingly popular to segment low-contrast images,[23–25] but they are very dependent on their input quality (*i.e.* the training set) and therefore prone to user-bias. The contrast of the carbon fibers has been improved by gold sputtering prior to weaving or soaking the fiber tows in iodine solution, though the latter stiffens the tows significantly.[26] Carbon fibers have also been mixed with glass fibers, which intrinsically have a better CT contrast with the polymer matrix.[26,27] However, their larger fiber diameter compared to carbon fibers results in a higher bending stiffness, leading to compatibility issues.[26]

Digital Image Correlation (DIC) is a non-contact measurement technique used to calculate displacements and strains of a variety of materials.[28,29] A random grey intensity distribution (*i.e.* a speckle pattern) is applied to the surface of the sample.[30] Digital images are then taken before and after deformation of the sample. By tracking the speckle displacement with correlation-based algorithms, full-field displacement can be calculated.[29] Following the success of DIC, a direct 3D extension was developed, called Digital Volume Correlation (DVC).[31,32] DVC has the advantage that it can visualize the internal volume and deformation behavior, by tracking the movement of small volume units within the sample, see Figure.[33] CT data is typically used to visualize the 3D volume, allowing researchers to measure how a material deforms and strains internally when subjected to loads. The possibility of timelapse CT imaging allows measuring the strains *in situ* via DVC. Initial CT-based DVC applications were focussed on biomechanics, mostly determination of failure structures in vertebra.[31] The technique has since been expanded to foams, soil, rocks, battery electrodes and more. Where DIC applies a surface speckle pattern, DVC relies on

https://doi.org/10.26434/chemrxiv-2024-cl440 **ORCID:** https://orcid.org/0000-0002-4653-7570 Content not peer-reviewed by ChemRxiv. **License:** CC BY-NC-ND 4.0

an internal pattern, which is either achieved by the naturally occurring texture within the sample or by adding markers with sufficiently different X-ray attenuation coefficients.[34–36] CT-based DVC is particularly of interest for FRPs, as it can determine both the direction and magnitude of internal strains. This makes it possible to differentiate between inter-, intra- or translaminar failure modes, which can not be achieved with other characterization techniques.[37?] In GFRPs the glass fibers are used as internal markers,[38,39] but for CFRPs the poor contrast between the carbon fibers and the polymer matrix makes this route challenging. The carbon fibers lack a trackable contrast pattern, leading to poor tracking and inaccurate displacement estimates.[38] Consequently there are relatively few studies using DVC on CFRPs and those that exist rely either on synchrotron CT scanning[40–42] or deep learning approaches.[23] Some studies have added nano- or microparticles to the matrix as high contrast trackers, though obtaining a homogeneous dispersion and avoiding a drastic viscosity increase is challenging.[41,43]

Here, we introduce HfO_2 NCs as CT contrast agents for CFRPs by coating the carbon fiber fabric with the NCs. Stable NC dispersions were obtained in chloroform at concentrations as high as 300 mg mL^{-1} with oleic acid as a surface ligand. These NC suspensions were employed to dipcoat the carbon fibers, using a combination of multiple layers with controlled dwell time, immersion- and withdrawal speed to obtain a homogeneous layer on the fiber surface. The NC-dipcoated CFRPs demonstrate significant contrast difference between tows, which scales with increased coating concentration. The improved CT contrast allows for straightforward and accurate segmentation of the different yarns. Furthermore, a mesh of NC-airbrushed squares on top of the fibers can be tracked in 3D after lateral displacement and segmented in micro-CT. The NCs can therefore be used as internal DVC trackers. The enhanced visualization leads to accurate geometry modelling, while DVC results in strain mapping of the composite under stress. Together they lead to a deeper understanding of CFRP behavior and therefore improved composite materials.

https://doi.org/10.26434/chemrxiv-2024-cl440 **ORCID:** https://orcid.org/0000-0002-4653-7570 Content not peer-reviewed by ChemRxiv. **License:** CC BY-NC-ND 4.0

Results and discussion

Colloidal HfO_2 NC synthesis

Hafnium oxide nanocrystals (HfO_2 NCs) are synthesized via our previously reported[44] gram-scale microwave-assisted solvothermal synthesis, starting from $HfCl_4$.2THF in benzyl alcohol, see Figure 1A. The NCs are functionalized post-synthesis with oleic acid as it is widely used, relatively cheap and does not interact well with epoxy. The latter is advantageous since a sharp contrast difference is necessary. The NCs should thus adhere well to the fiber surface and not be absorbed in the surrounding epoxy polymer interface. Broadened ^{1}H nuclear magnetic resonance (NMR) peaks, shown in Figure 1B, are indicative of bound ligands and show good purification. Figure 1C displays the transition electron microscopy (TEM) image. The NCs have an ellipsoidal size with a major axis of 6.2 ± 4.8 nm and minor axis of 4.0 ± 2.4 nm ($\mu \pm 3\sigma$).

Oleic acid provides stability in a wide range of nonpolar solvents.[45–47] We opt for chloroform, a fast-drying (boiling point = 61 °C) and low-viscosity (0.54 mPa.s at 25 °C) solvent, therefore less likely to form the wedge shaped coating characteristic to dipcoating. Dynamic light scattering (DLS) is used to determine the solubility of oleate-functionalized HfO_2 NCs (HfO_2/OA) in chloroform at increasing concentration. Figure 1D shows the volume size distributions of HfO_2/OA measured at concentrations between 1 and 300 mg mL^{-1} (ligand weight of 15 m% not taken into account). There is no observed shift in solvodynamic diameter with increasing concentrations. The corresponding Z-average diameter, which is most sensitive to agglomeration, is shown in Figure 1E. A slight increase with increasing concentration is observed, reaching 34 ± 1.5 nm ($\mu \pm 3\sigma$) for 300 mg mL^{-1}. With a main (99.9 vol%) peak still located at 17 ± 11 nm we can conclude that the particles are well-dispersed even at the highest concentration. The HfO_2/oleate NCs in chloroform are therefore an optimal candidate for dipcoating. An overview of all calculated DLS values is given in Table S1.

https://doi.org/10.26434/chemrxiv-2024-cl440 **ORCID:** https://orcid.org/0000-0002-4653-7570 Content not peer-reviewed by ChemRxiv. **License:** CC BY-NC-ND 4.0

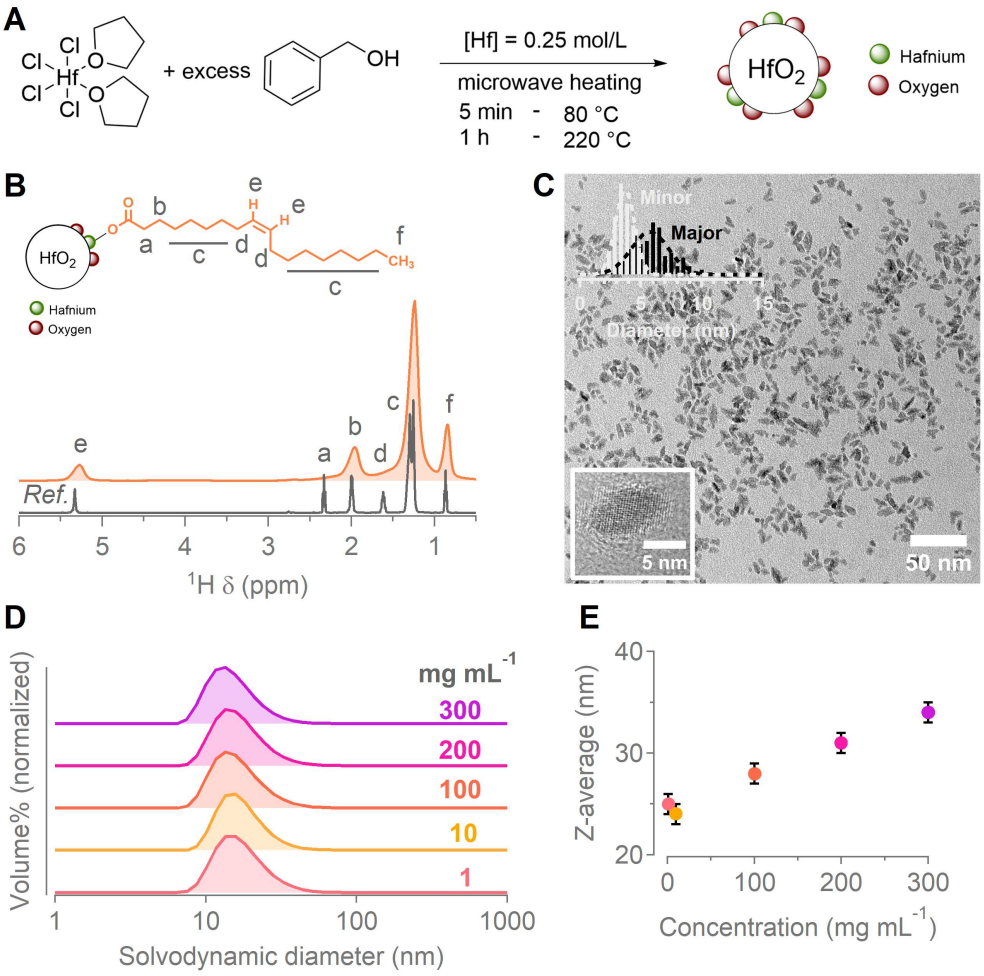

Figure 1: (A) Synthesis reaction scheme of HfO_2 NCs starting from $HfCl_4$.2THF in benzyl alcohol. (B) ^{1}H NMR spectrum of HfO_2 NCs functionalized with oleic acid (orange, broad resonances) compared to a reference spectrum of the free ligand (grey, sharp resonances). (C) TEM image of the NCs with size distribution and a zoom of a single NC shown in the top and bottom left corner respectively. (D) DLS volume size distribution of HfO_2/OA NCs in chloroform at concentrations ranging from 1 to 300 mg mL^{-1}. (E) Z-average diameters as determined by DLS in function of increasing concentration.

https://doi.org/10.26434/chemrxiv-2024-cl440 **ORCID:** https://orcid.org/0000-0002-4653-7570 Content not peer-reviewed by ChemRxiv. **License:** CC BY-NC-ND 4.0

Dipcoating of carbon fibers

In order to avoid micro-CT artifacts, the HfO_2 NCs should be homogeneously dispersed on the carbon fiber surface. The fiber sizing is often removed before dipcoating fibers[17,48,49] and could be stripped by overnight reflux in acetone (Figure S1). While this step introduces additional time and effort, no impact on the adhesion of the NCs was observed. We therefore conclude that sizing removal has no advantage and should be left intact.

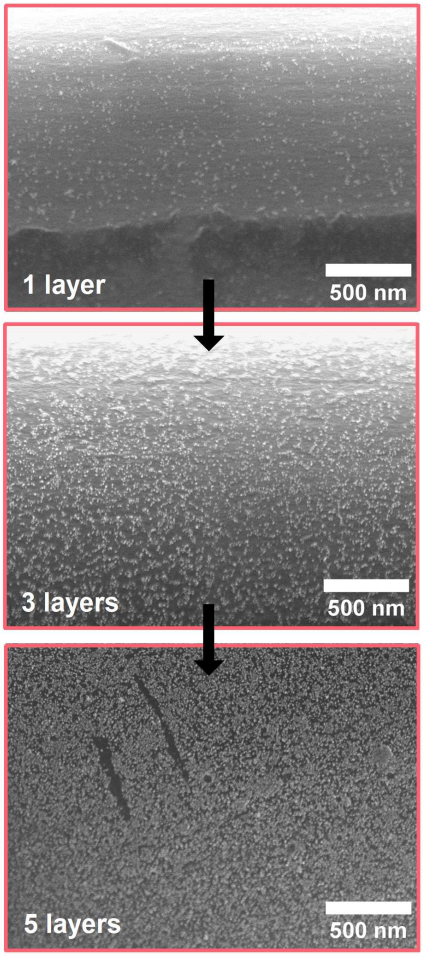

Figure 2: SEM image of the carbon fiber surface, coated with 1 mg mL^{-1} HfO_2 NCs. Increased layers causes more NCs to be deposited, creating a near-monolayer after 5 layers.

Scanning Electron Microscopy (SEM) data, shown in Figure 2, is used to confirm the presence of the HfO_2 NCs on the carbon fiber surface. Single fibers are randomly extracted from the NC-dipcoated fiber bundle and assumed representative for the whole sample. Figure

https://doi.org/10.26434/chemrxiv-2024-cl440 **ORCID:** https://orcid.org/0000-0002-4653-7570 Content not peer-reviewed by ChemRxiv. **License:** CC BY-NC-ND 4.0

S2 shows a layered SEM image of hafnium mapping on the fiber surface, detected via energy dispersive X-ray analysis (EDX), confirming that the observed particles on the fiber surface are the HfO_2 NCs. The dipcoating parameters (immersion speed, dwell time and withdrawal speed) were coarsely evaluated, as visualized in Figure S3. While limited to visual comparison of the SEM images, some conclusions can be drawn based on the amount of deposited NCs. Increased withdrawal speed increases the concentration of nanocrystals deposited on the fibers due to the reduced flow back in solution during drainage. An effect was also observed for the immersion speed and dwell time, where slower speeds and longer immersion times create a higher concentration. Re-coating the same carbon fiber fabric using the optimized parameters lead to a denser coating than could be obtained by a single, slow dip. At five layers, the complete fiber surface is covered with individually dispersed particles. The combination of NC concentration and number of coatings allows to tune the dispersion of NCs over a wide range using the optimized dipcoating parameters. The reproducibility of the obtained coating with the same parameters was confirmed in Figure S4. To verify the absence of a coating gradient, SEM images were taken at the top and bottom of a NC-dipcoated carbon fiber bundle, showing an equal NC concentration on the fiber, see Figure S5. Other nonpolar solvents such as hexane and toluene resulted in more heterogeneous coatings compared to those obtained with chloroform, as shown in Figure S6.

Proof-of-concept of coated fibers

Having obtained a homogeneous coating with various concentrations, the CT contrast enhancement was evaluated by dipcoating carbon fiber bundles with 1, 10 or 100 mg mL^{-1} NCs in chloroform. Each bundle was dipcoated five consecutive times to obtain dense coatings, according to the parameters determined above. Figure 3A shows the corresponding SEM data of the NC-dipcoated carbon fibers with increasing concentrations. The carbon fiber bundles were added to epoxy resin and cured. The resulting proof-of-concept samples were

https://doi.org/10.26434/chemrxiv-2024-cl440 **ORCID:** https://orcid.org/0000-0002-4653-7570 Content not peer-reviewed by ChemRxiv. **License:** CC BY-NC-ND 4.0

analyzed via micro-CT using a peak tube potential of 90 kV and voxel sizes between 5^3 and 17 μm^3. Compared to the reference sample with no NCs, a significant improvement in contrast can be observed in cross-sections of the micro-CT scans compared to the reference sample (Figure 3B). As carbon fibers are naturally slightly more attenuating than the epoxy matrix, a minor contrast difference is also observed in the reference (0 mg mL^1) sample. It is insufficient to automatically extract the complete fiber bundle via region growing segmentation, as seen in the inaccurate segmentation results. However, already at a NC concentration of 1 mg mL^{-1}, the contrast improvement suffices to automatically and accurately segment the complete carbon fiber bundle. Additional SEM and CT data is given in Figure S7, together with the 3D rendered volumes of the samples with extracted fiber bundles.

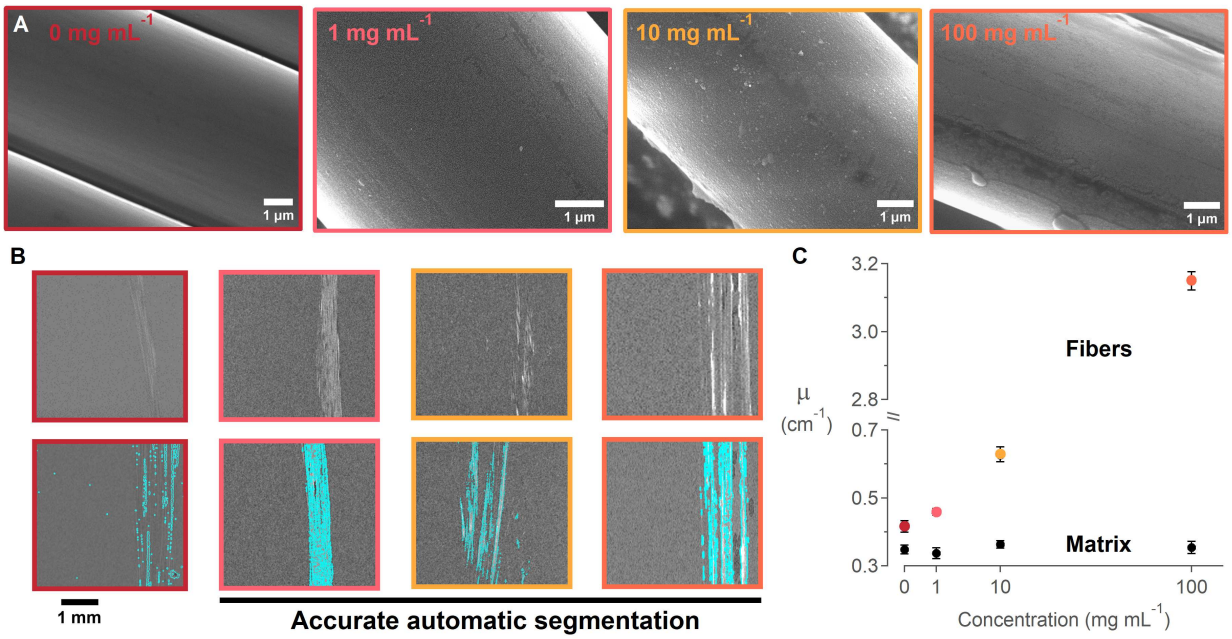

Figure 3: Contrast-enhancement of HfO_2 NC-dipcoated CFRPs with increasing concentration of NCs. (A) SEM images of the fibers dipcoated with, from left to right, 0, 1, 10 and 100 mg mL^{-1} NCs. (B) Cross-section micro-CT scan slices containing one fiber bundle (top) with region-growing segmentation results highlighted in blue (bottom). (C) Linear attenuation coefficient of the fibers and the polymer matrix shows increasing contrast difference with increasing concentration. Note that the y-axis is zoomed in to visualize the error bars.

The linear attenuation coefficient μ (cm^{-1}) of the fibers increases in function of NC dipcoating concentration, see Figure 3C. As the attenuation coefficient of the (undoped) epoxy

https://doi.org/10.26434/chemrxiv-2024-cl440 ORCID: https://orcid.org/0000-0002-4653-7570 Content not peer-reviewed by ChemRxiv. License: CC BY-NC-ND 4.0

matrix remains constant, the attenuation difference, *i.e.* the contrast, thus scales with increasing concentration.

Contrast-enhanced NC-dipcoated interface

Having determined the minimum concentration needed for semi-automatic segmentation, NC-dipcoated CFRPs were manufactured using the concentrations of 1, 10 and 100 mg mL^{-1} suspensions of HfO_2/OA in chloroform. Laminates were made of nine layers of woven carbon fiber fabric. To validate contrast-enhancement, the three middle layers were coated with HfO_2 NCs, while the three top and bottom layers are left uncoated. The middle carbon fiber fabric layers were dipcoated five times according to Figure 2. The final laminate stack was infused using vacuum-assisted resin infusion (VARI). The epoxy polymer flow during vacuum infusion does not remove the NC-coating on the fibers, as comparison of samples take from the bottom, middle and top of the laminate show no decrease in attenuation, see Figure S8. Small samples (3 x 3 mm) were diamond cut to use as representative unit cell (RUC), the small repeatable volume that statistically represents the structure. These samples were scanned in micro-CT using a tube potential of 90 kVp and a voxel size of 3.5^3 μm^3.

Cross-section slices of the NC-dipcoated CFRPs are shown in Figure 4A. Videos going through the complete samples are supplied in the Supporting Information. Fibers coated with 1 mg mL^{-1} NC concentration show a distinguishable, though minor contrast improvement. Interestingly the NCs penetrate within the fiber fabric as well, enhancing the throughout the entire tow. In the accompanying greyscale histogram the uncoated fibers cannot be distinguished from the coated fibers (Figure 4B). A more drastic contrast improvement is noted for the 10 and 100 mg mL^{-1} NC concentrations. The interface shows a sharp contrast going from the resin-rich polymer regions to the NC-dipcoated fiber fabric, which is absent in the uncoated layers. For the 10 mg mL^{-1} NC-dipcoated CFRP the peaks in the greyscale

https://doi.org/10.26434/chemrxiv-2024-cl440 **ORCID:** https://orcid.org/0000-0002-4653-7570 Content not peer-reviewed by ChemRxiv. **License:** CC BY-NC-ND 4.0

histogram still overlap, but the 100 mg mL^{-1} histogram displays a shift in the peak associated with the coated fiber tows.

To demonstrate the contrast difference, the dipcoated carbon fiber tows are segmented using the region-growing approach, see Figure 4C. This semi-automatic segmentation can extract 1 mg mL^{-1} NC-dipcoated fibers from uncoated fibers and extract the NC-dipcoated fibers from the polymer matrix. Segmentation of the interface between tows is more straightforward with the 10 and 100 mg mL^{-1} NC-dipcoated fibers due to the excess of NCs present on the tows. Some 3D rendered volumes of both samples are given with the segmented fibers highlighted. Interestingly, a simple thresholding approach struggles to distinguish the interface in the 1 mg mL^{-1} dipcoated fibers, but can easily extract the 10 and 100 mg mL^{-1} dipcoated fiber interfaces, evident of their stark shift in contrast, see Figure S9. Figure S10 shows micro-CT data of a reference sample with no coated fibers present. The region-growing approach cannot distinguish fibers from matrix or extract interfaces between tows. A laminate with the complete fiber fabric coated with 1 mg mL^{-1} is given by comparison, where the region-growing segmentation could roughly extract the fiber fabric from the polymer matrix.

https://doi.org/10.26434/chemrxiv-2024-cl440 **ORCID:** https://orcid.org/0000-0002-4653-7570 Content not peer-reviewed by ChemRxiv. **License:** CC BY-NC-ND 4.0

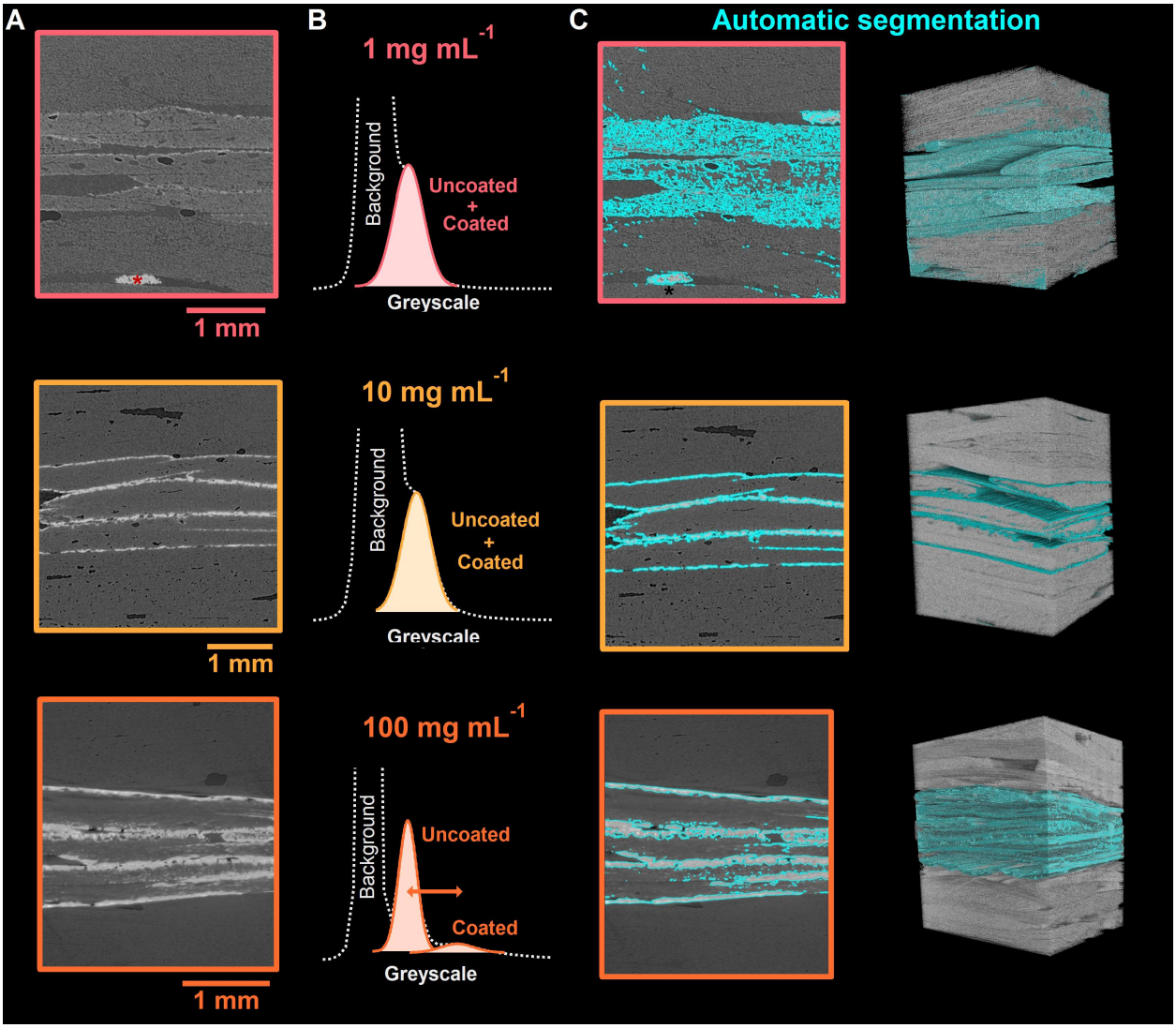

Figure 4: Cross-section slice of micro-CT scan shows the contrast enhancement of NC-coated fibers with (A) 1 mg mL^{-1} and (B) 100 mg mL^{-1} HfO_2 NCs. Greyscale histograms with Gaussians fitted to the fiber contributions are shown. * denotes an impurity in the CFRP. Automatic segmentation of the micro-CT scan slice and 3D volume renders with (C) 1 mg mL^{-1} and (D) 100 mg mL^{-1}. The segmented fibers are highlighted.

https://doi.org/10.26434/chemrxiv-2024-cl440 **ORCID:** https://orcid.org/0000-0002-4653-7570 Content not peer-reviewed by ChemRxiv. **License:** CC BY-NC-ND 4.0

Nanocrystals for digital volume correlation

In comparison with dipcoating, HfO_2/OA NCs were also deposited on the carbon fibers using an airbrushing approach. A suspension of 250 mg mL^{-1} NCs was airbrushed on the woven carbon fiber fabric. SEM analysis shows a high NC concentration, see Figure 5A. NC-airbrushed CFRPs were manufactured similar to the previous section, with the middle three layers coated with NCs, while the top and bottom three layers are left uncoated. The laminate was also scanned using the same settings as previous, *i.e.* a tube potential of 90 kVp and voxel size of 3.5^3 μm^3. There is a clear greyscale difference on the NC-airbrushed fiber layers, marking the interface between tows, see Figure 5B. The greyscale profile throughout a micro-CT scan slice shows sharp spikes in intensity corresponding to each layer, see Figure S11B. Region growing segmentation can easily extract the interface of the NC-airbushed layer with high accuracy, as shown in Figure 5C. The interface can also be differentiated via thresholding segmentation, see Figure S11C.

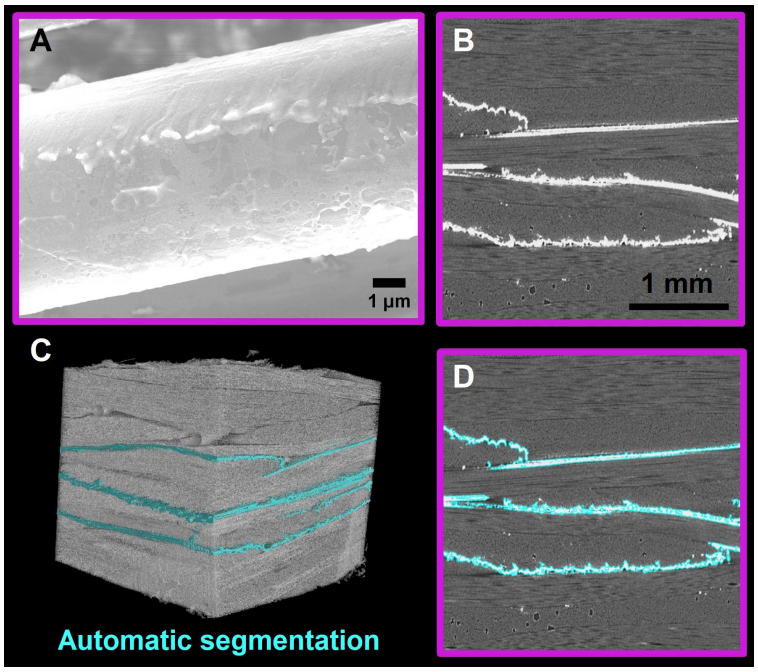

Figure 5: Airbrushing of carbon fibers with a suspension of HfO_2 NCs. (A) SEM image of fiber airbrushed with NCs. (B) Cross-section slice of micro-CT scan shows the contrast enhancement at the interface. (C) Automatic segmentation of the micro-CT scan slice and 3D volume render. The segmented layers are highlighted.

https://doi.org/10.26434/chemrxiv-2024-cl440 **ORCID:** https://orcid.org/0000-0002-4653-7570 Content not peer-reviewed by ChemRxiv. **License:** CC BY-NC-ND 4.0

The main advantage of airbrushing lies in its flexibility to selectively coat certain regions. Using a lasercut mesh, squares of 0.5 x 0.5 mm^2 were airbrushed on the carbon fiber surface using a HfO_2 NC concentration of 250 mg mL^{-1}, as illustrated in Figure S12A. The layered SEM-EDX image with hafnium mapping confirms the successful patterning of the squares with the NCs (Figure 6A). The pattern is recognizable in X-ray radiography, see Figure 6B, which makes it suitable as internal marker in digital volume correlation (DVC) tracking. A laminate was constructed of six woven carbon fiber fabric layers, with the mesh applied on the second layer from the top, the stacking is illustrated in Figure S12B. The composite was scanned at a tube potential of 90 kVp and voxel size of 18^3 μm^3. Figure 6C shows the side view on a micro-CT scan slice. The squared pattern is easily recognized and could be extracted due to its higher contrast. In the 3D rendered volumes, the segmented squares are highlighted in blue. The peaks associated to the fibers and the coated squares are well-separated in the corresponding greyscale histogram (Figure S13). The greyscale profile throughout the scan is constant, except for an intense spike when the NC-airbrushed squares are encountered, see Figure S14.

The potential of the squares as internal speckle pattern in DVC is demonstrated in Figure 6D. The laminate was scanned in micro-CT, together with a reference object, see Figure S15A. Afterwards the complete laminate was laterally displaced compared to the reference object and rescanned using the same settings. Post-processed alignment of the reference object shows the displacement of the unique squares, which could readily be traced. A section of the complete sample is shown here, Figure S15B shows the complete laminate. Preliminary experiments have shown no influence of the NCs on the mechanical properties of the laminate, as such the trackers will not affect the DVC results.

https://doi.org/10.26434/chemrxiv-2024-cl440 **ORCID:** https://orcid.org/0000-0002-4653-7570 Content not peer-reviewed by ChemRxiv. **License:** CC BY-NC-ND 4.0

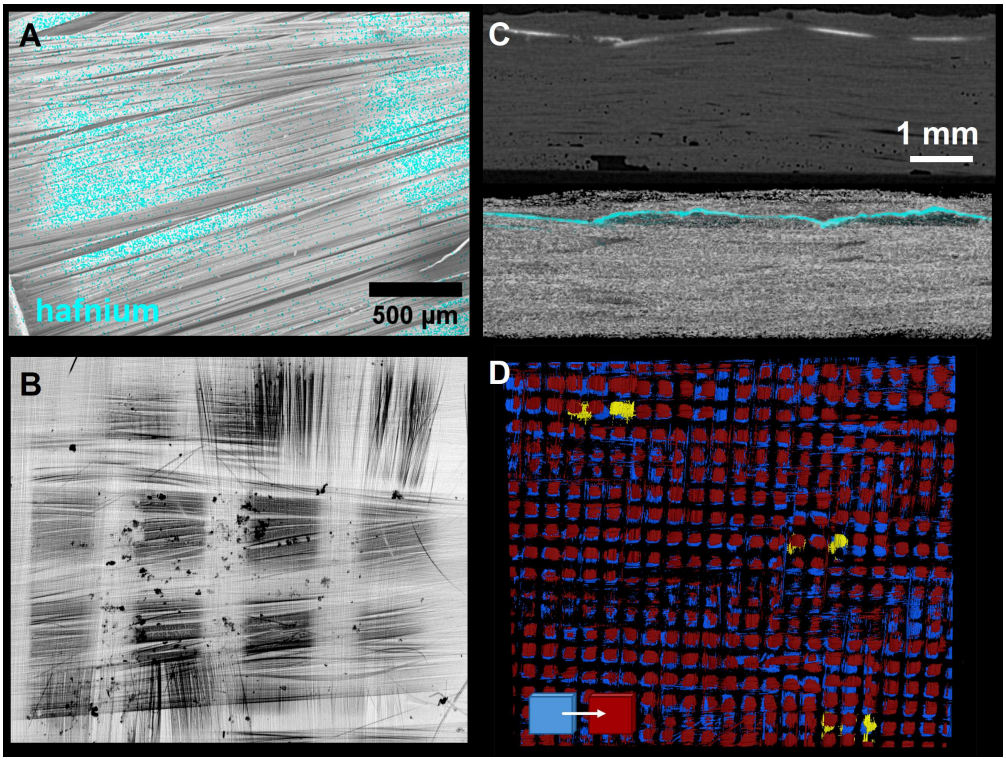

Figure 6: (A) Illustration of airbrushing on the fibers using a mesh of 0.5 x 0.5 mm squares. (B) Layered SEM-EDX image of the hafnium distribution on the fibers. (C) Radiograph of mesh of NCs on the fibers. (D) Cross-section slice of micro-CT scan (top) and 3D volume render with segmented fibers (bottom). (E) Greyscale histogram with Gaussians fitted to the fiber contributions. (F) 3D volume renders after shifting the sample. The top left corner illustrates the position of the samples relative to each other.

Conclusion

A better understanding of any materials' behavior starts by simply looking at its structure. For CFRPs, the internal structure has been virtually unattainable, as visualization using micro-CT is challenging due to the poor contrast between the carbon fibers and the polymer matrix. Here, we present visualization of the interface between tows by coating the fibers with HfO_2 NCs. Stable dispersions were obtained at a wide range of concentrations by functionalization of the HfO_2 surface with oleic acid in chloroform. Solution dipcoating was used to coat the carbon fibers. By tuning the concentration, amount of layers, dipcoating speeds and dwell time, a homogeneous monolayer of NCs on the carbon fiber tows was obtained. Proof-of-concept CT analysis showed that preferably a concentration of minimum 10 mg

https://doi.org/10.26434/chemrxiv-2024-cl440 **ORCID:** https://orcid.org/0000-0002-4653-7570 Content not peer-reviewed by ChemRxiv. **License:** CC BY-NC-ND 4.0

mL^{-1} NCs is sufficient for semi-automatic segmentation of the fiber bundles. NC-airbrushed CFRP laminates were made with 1, 10 and 100 mg mL^{-1} NC concentrations and showed significant enhancement of CT contrast on the interface. Semi-automatic segmentation via region-growing was possible on all samples, though it was more straightforward with increasing NC concentration. Contrast improvement was also obtained by airbrushing on the carbon fibers tows. We demonstrate the use of a mesh of NC-airbrushed squares as internal tracker in DVC. The squares can be distinguished from the laminate and correlated after lateral displacement. This enables the possibility for DVC on CFRPs. The HfO_2 NC-airbrushed fibers thus create the possibility to both look at and understand the internal structure of CFRPs, a first step towards a better understanding of their damage behavior.

Experimental

Materials

Hafnium(IV) chloride (98%), oleic acid (90%), oleylamine (70%) and chloroform (stabilized with amylenes, ≥99%) were purchased from Sigma-Aldrich. Benzyl alcohol was either purchased anhydrous (99.8%) or as ReagentPlus® (≥99%) from Sigma-Aldrich, the latter was then vacuum distilled (55 °C at 35 mTorr) and stored over sieves in a glovebox under inert atmosphere. $CDCl_3$ was purchased from Eurisotop and stored over sieves. Tetrahydrofuran (ExtraDry, 99.5%) was purchased from Acros Organics. Marbocote 227 CEE release agent was purchased from Fatol-Kunststoffen. Epikote™ resin MGS RIMR135 and Epikure™ curing agent MGS RIMH137 were purchased from Hexion. Chemlease® 41-90 EZ was purchased from Chem-Trend. Wrightlon® 7400 nylon vacuum bagging film, Wrightlon® 5200 high performance fluoropolymer release film, Resinflow 100 resin distribution medium and ultraweave® 606 medium weight nylon breather/bleeder were purchased from Airtech Europe SARL. Aerofilm® PP180 economy polyester peel ply and ST150 vacuum bagging gum sealant tape were purchased from EasyComposites. Solvents used for synthesis were

https://doi.org/10.26434/chemrxiv-2024-cl440 ORCID: https://orcid.org/0000-0002-4653-7570 Content not peer-reviewed by ChemRxiv. License: CC BY-NC-ND 4.0

purchased from Chemlab or Sigma-Aldrich. All manipulations are performed in air unless otherwise indicated. All chemicals are used as received unless otherwise mentioned. When required, organic solvents are dried according to the procedure described by Williams et al.[50] making use of 20% m/v freshly activated 3Å sieves for a minimum of 120 h.

$HfCl_4$.2THF synthesis

In a glovebox under inert atmosphere (nitrogen or argon), 22 g of $HfCl_4$ (1 eq, 0.069 mol) is added to 330 mL anhydrous DCM, only partly dissolving, thereby rendering a turbid solution. Next, 22 mL (3.95 eq, 0.271 mol, 19.56 g) of anhydrous THF is added in a dropwise manner and under vigorous stirring. The $HfCl_4$ dissolves completely during addition of the THF. 220 mL anhydrous pentane is added, carefully pouring along the sides and the solution is left in the freezer (- 18 °C) for 2 hours to recrystallize. The resulting powder is filtered over a por 4 filter funnel and washed with pentane. The free flowing white powder is dried under vacuum, resulting in a chemical yield of 89%.

Gram-scale microwave-assisted HfO_2 nanocrystal synthesis

Precursor preparation is executed in a nitrogen-filled glovebox. 40 mL anhydrous benzyl alcohol (38 eq, 0.38 mol, 41.6 g) is added to the liner of the EasyPrep Plus vessel. 4.65 g $HfCl_4$.2THF (1 eq, 0.01 mol) is carefully and slowly added to the liner under vigorous stirring. The edges of the liner are rinsed with the solution via a syringe to remove any powder stuck to the edge. Up to three liners can be added simultaneously to the microwave. The solution is stirred for 5 minutes, resulting in a transparent solution. The mixtures are subjected to microwave heating for 5 minutes at 80 °C (10 minute ramp, power = 200W), followed by 1 hour at 220 °C (20 minute ramp, power = 800W). After synthesis, the liners are opened and 5 mL water is added together with 200 μL HCl (37 w/w%). Sometimes the solvent is yellow instead of transparent, this does not affect the quality of the particles. The content is transferred to a separating funnel. Each liner is rinsed with 30 mL diethyl ether,

https://doi.org/10.26434/chemrxiv-2024-cl440 ORCID: https://orcid.org/0000-0002-4653-7570 Content not peer-reviewed by ChemRxiv. License: CC BY-NC-ND 4.0

which is also added to the funnel. The mixture was shaken and allowed to separate for 15 minutes. The bottom (aqueous) phase is collected in a flask and 10 mL ethanol is added to the solution. 25 mL diethyl ether is added and the precipitated NCs are filtered over a por 5 filter under vacuum with a grade 1 filter paper added.The particles are redispersed in 5 mL chloroform. Under stirring, 750 μL oleic acid (0.24 eq, 0.0024 mol, 0.668 g) is added, followed by 625 μL oleylamine (0.19 eq, 0.0019 mol, 0.506 g). The mixture is subjected to sonication for 30 minutes. In some cases the mixture remained turbid after addition of the ligands, but will be transparent upon redispersion after the washing step. 25 mL of acetone is added and the particles are filtered over a por 5 filter with vacuum paper. Additional acetone was used to wash the particles. Chloroform can be used to remove all particles from the filter.

Dipcoating of carbon fiber fabric with HfO_2 nanocrystals

Dipcoating is done using a KSV instruments LTD dipcoater. For single fiber bundles, a vial was used as reservoir. To minimize solvent and HfO_2 NCs needed, a custom Teflon reservoir was made to dipcoat woven carbon fiber bundles used for the laminates. An illustration of the reservoir is shown in Figure S16, with measurements indicated. Edges of the carbon fiber fabric were glued with a two-component epoxy glue to avoid unraveling of the fibers during dipcoating and left to dry for a minimum of one hour. Samples were dipcoated with an immersion speed of 50 mm min^{-1}, dwell time of 5 minutes and a withdrawal speed of 100 mm min^{-1}. When multiple coatings were applied to the same substrate, a wait period of 1 min was used between coatings and the dwell time for the subsequent layers reduced to 30 seconds. Afterwards the fibers were dried overnight in an oven at 80 °C.

Airbrushing of carbon fiber fabric with HfO_2 nanocrystals

Airbrushing was done using a dual-action airbrush. The reservoir is loaded with the NC suspension and the compressed air set to 2 bar. The airbrush was kept at a distance of

https://doi.org/10.26434/chemrxiv-2024-cl440 ORCID: https://orcid.org/0000-0002-4653-7570 Content not peer-reviewed by ChemRxiv. License: CC BY-NC-ND 4.0

approximately 10 cm and maximum feeding rate, going twice over the fiber fabric to ensure full coating. For the DVC trackers, a mesh was made from a mylar (PET) A4 foil with a thickness of 0.3 mm. The 0.5 x 0.5 mm squares were laser cut using a BRM 90130 100W laser cutter. The mesh was taped over the carbon fiber fabric before airbrushing.

Nanocrystal-coated carbon fiber reinforced polymer formation

Laminates are made using vacuum-assisted resin infusion (VARI). The laminate set-up is illustrated in Figure Sxx. On a clean 15 x 25 cm glass plate, a section of 6.5 x 13.5 cm was taped off and three layers of release agent (Chemlease®) were applied with a 10 minute wait time between each layer, after which the tape marking is removed. The layers of 5 x 8 cm carbon fiber woven fabric were stacked on the section coated with release agent. A peel ply fabric (5 x 10 cm) and semi-perforated release film (5 x 10 cm) was placed on top and the stacking was taped down. An inlet (ca. 30 cm) and outlet (ca. 90 cm) tube was added with plastic T-sections wrapped in bleeder fabric. A vacuum bag of 20 x 30 cm with vacuum tape along the edges was added over the stacking, not on the release agent section. Small folds above and below the inlet and outlet tubes were used. The inlet tube was clamped and the outlet tube applied to vacuum. The outlet tube was clamped as well. If this held for 24 hours without losing vacuum, the set-up was infused. 100 g of Epikote™ resin was thoroughly mixed with 30 g of Epikure™ curing agent. The outlet tube was connected to the vacuum through a resin trap and the inlet tube added to the resin mixture. The set-up was infused under vacuum. After clamping the inlet and outlet tubes, the laminate was cured for 24 h at room temperature, followed by 15 h at 80 °C in a Naberthem P330 oven. After curing, the vacuum bag, tubes, peel ply and release film were removed and the laminated was released from the glass plate.

https://doi.org/10.26434/chemrxiv-2024-cl440 **ORCID:** https://orcid.org/0000-0002-4653-7570 Content not peer-reviewed by ChemRxiv. **License:** CC BY-NC-ND 4.0

Micro-CT scans

Micro-computed tomography was done at the Ghent University Centre for X-ray Tomography (UGCT) using the HECTOR[51] and CoreTom scanner. Samples were scanned in cone-beam mode. OCTOPUS reconstruction software version 8.9 was used to obtain a stack of reconstructed TIFF images. The proof-of-concept concentration series was scanned at a voxel size of 5^3 (for 100 mg mL^{-1}), 10^3 (for 1 and 10 mg mL^{-1-}) and 17^3 (for 0 mg mL^{-1}) μm^3, the composite laminates at a voxel size of 3.5^3 and 18^3 μm^3. All were scanned at 90 kVp tube potential and a power of 10 W. No hardware filter was applied. 2400 projections were taken using 1000 ms exposure time per projection. The radiography image was taken at 90 kVp tube potential and a power of 10 W with 20 times 1000 msec exposure time.

CT scan postprocessing and region growing segmentation

Datasets were processed using the VGStudio Max software. CT scans were imported as an image stack. The fibers were segmented from the surrounding matrix by creating a selection using the automatic region growing (flooding) algorithm. A seed point was manually placed in any of the 2D views after which the algorithm grows the selection, continuously expanding as long as the neighboring voxels are within the user-specified tolerance relative to the seed. The region growing algorithm was used in static mode, *i.e.* voxels are added to the selection if they are connected to the region and if their greyvalues do not deviate by more than the chosen tolerance from the greyvalue of the seed point. No other constraints (such as max. radius) where applied to algorithm. The tolerance value and seed point were changed until an optimal selection was obtained. For some data, the Opening/Closing mode is applied, which eliminates gaps in the selection that was grown by expanding the selection with the user-specified number of voxels and then immediately contracting. Finally, the selection is extracted from the volume as a separate region-of-interest (ROI). The 3D volume render was exported as an image as isosurface render, displaying the surface of the selected ROI as defined by the manually set iso-level. Histograms and thresholding were obtained by

https://doi.org/10.26434/chemrxiv-2024-cl440 **ORCID:** https://orcid.org/0000-0002-4653-7570 Content not peer-reviewed by ChemRxiv. **License:** CC BY-NC-ND 4.0

ImageJ/Fiji.

SEM analysis

Scanning electron microscopy (SEM) was performed using a JEOL FEG SEM JSM-7600F at an accelerating voltage of 10 kV in secondary electron mode. Energy dispersive X-ray spectroscopy (EDX) was done using an Oxford Instruments X-Max 50 SDD EDX detector.

TEM analysis

High-resolution transmission electron microscopy (HRTEM) was performed on a JEOL JEM-2200FS TEM with Cs corrector operating at 200 kV. Samples were made by drop-cast suspension on the grids. The TEM grids used were Holey-Carbon - Cu (C200-CU) with 50 micron hole size (200 mesh). NC sizes were determined by measuring 200 particles using the polygon selection tool of ImageJ, with measurements set to fit ellipse.

NMR analysis

Nuclear magnetic resonance (NMR) spectra were recorded at 298.15K on a Bruker 300 instrument at 400 MHz. Chemical shifts (δ) are given in parts per million (ppm) and the residual solvent peak was used as an internal standard ($CDCl_3$: δH = 7.24 ppm). All resonances are background corrected. Coupling constants are reported in Hertz (Hz). ^{1}H spectra were acquired using the standard zg30 pulse sequence from the Bruker library.

DLS analysis

Dynamic Light Scattering (DLS) measurements were recorded on a Malvern Zetasizer ZS instrument in backscattering mode (173°) at a temperature of 20 °C using a 60 second equilibration time. Nanocrystals were measured in glass cuvettes and each measurement

https://doi.org/10.26434/chemrxiv-2024-cl440 **ORCID:** https://orcid.org/0000-0002-4653-7570 Content not peer-reviewed by ChemRxiv. **License:** CC BY-NC-ND 4.0

was repeated 6 times. DLS data processing was performed using the Malvern ZS Explorer software using the general purpose analysis model.

Acknowledgement

The authors gratefully acknowledge the Research Foundation-Flanders (Project No. 1S11721N and 1163125N), Ghent University and the University of Basel for financial support. The special research fund of the Ghent University (BOF-UGent) is acknowledged for the financial support of the UGCT Core Facility (BOF.COR.2022.008) and the Concerted Research Actions project (BOF2015/GOA/007). TEM measurements were performed at the UGent TEM Core Facility. We thank I. De Baere for composite sample preparation and discussions, K. Van Houtte for lasercutting, I. Josipovic for micro-CT measurements and E. Picavet for additional SEM measurement. The TOC graphic was partly created using BioRender.com.

Supporting Information Available

Supporting information contains additional SEM data, CT data, visualizations of the set-up and table with DLS results.

References

(1) Hiremath, N.; Young, S.; Ghossein, H.; Penumadu, D.; Vaidya, U.; Theodore, M. Low cost textile-grade carbon-fiber epoxy composites for automotive and wind energy applications. *Composites Part B: Engineering* **2020**, *198*, 108156.

(2) Soutis, C. Fibre reinforced composites in aircraft construction. *Progress in aerospace sciences* **2005**, *41*, 143–151.

(3) Wazeer, A.; Das, A.; Abeykoon, C.; Sinha, A.; Karmakar, A. Composites for electric

https://doi.org/10.26434/chemrxiv-2024-cl440 **ORCID:** https://orcid.org/0000-0002-4653-7570 Content not peer-reviewed by ChemRxiv. **License:** CC BY-NC-ND 4.0

vehicles and automotive sector: a review. *Green Energy and Intelligent Transportation* **2022**, 100043.

(4) Petrou, M. F.; Parler, D.; Harries, K. A.; Rizos, D. C. Strengthening of reinforced concrete bridge decks using carbon fiber-reinforced polymer composite materials. *Journal of Bridge Engineering* **2008**, *13*, 455–467.

(5) He, C.; Yu, R.; Sun, H.; Chen, Z. Lightweight multilayer composite structure for hydrogen storage tank. *International Journal of Hydrogen Energy* **2016**, *41*, 15812–15816.

(6) Eyckens, D. J.; Stojcevski, F.; Hendlmeier, A.; Randall, J. D.; Hayne, D. J.; Stanfield, M. K.; Newman, B.; Vukovic, F.; Walsh, T. R.; Henderson, L. C. Carbon fibre surface chemistry and its role in fibre-to-matrix adhesion. *Journal of Materials Chemistry A* **2021**, *9*, 26528–26572.

(7) Sharma, M.; Gao, S.; Mader, E.; Sharma, H.; Wei, L. Y.; Bijwe, J. Carbon fiber surfaces and composite interphases. *Composites Science and Technology* **2014**, *102*, 35–50.

(8) Paredes, J.; Martinez-Alonso, A.; Tascon, J. Oxygen plasma modification of submicron vapor grown carbon fibers as studied by scanning tunneling microscopy. *Carbon* **2002**, *40*, 1101–1108.

(9) Chawla, K. K. *Composite materials: science and engineering*; Springer Science & Business Media, 2012.

(10) Thomason, J. L.; Adzima, L. Sizing up the interphase: an insider's guide to the science of sizing. *Composites Part A: Applied Science and Manufacturing* **2001**, *32*, 313–321.

(11) Tian, Y.; Zhang, H.; Zhang, Z. Influence of nanoparticles on the interfacial properties of fiber-reinforced-epoxy composites. *Composites Part A: Applied Science and Manufacturing* **2017**, *98*, 1–8.

https://doi.org/10.26434/chemrxiv-2024-cl440 **ORCID:** https://orcid.org/0000-0002-4653-7570 Content not peer-reviewed by ChemRxiv. **License:** CC BY-NC-ND 4.0

(12) Qin, W.; Vautard, F.; Askeland, P.; Yu, J.; Drzal, L. Modifying the carbon fiber–epoxy matrix interphase with silicon dioxide nanoparticles. *Rsc Advances* **2015**, *5*, 2457–2465.

(13) Liu, L.; Li, L.; Gao, Y.; Tang, L.; Zhang, Z. Single carbon fiber fracture embedded in an epoxy matrix modified by nanoparticles. *Composites science and technology* **2013**, *77*, 101–109.

(14) Qian, H.; Greenhalgh, E. S.; Shaffer, M. S.; Bismarck, A. Carbon nanotube-based hierarchical composites: a review. *Journal of Materials Chemistry* **2010**, *20*, 4751–4762.

(15) Zhang, X.; Fan, X.; Yan, C.; Li, H.; Zhu, Y.; Li, X.; Yu, L. Interfacial microstructure and properties of carbon fiber composites modified with graphene oxide. *ACS applied materials & interfaces* **2012**, *4*, 1543–1552.

(16) Godara, A.; Gorbatikh, L.; Kalinka, G.; Warrier, A.; Rochez, O.; Mezzo, L.; Luizi, F.; Van Vuure, A.; Lomov, S.; Verpoest, I. Interfacial shear strength of a glass fiber/epoxy bonding in composites modified with carbon nanotubes. *Composites Science and Technology* **2010**, *70*, 1346–1352.

(17) Wu, Q.; Zhao, R.; Liu, Q.; Jiao, T.; Zhu, J.; Wang, F. Simultaneous improvement of interfacial strength and toughness between carbon fiber and epoxy by introducing amino functionalized ZrO_2 on fiber surface. *Materials & Design* **2018**, *149*, 15–24.

(18) Tang, X.; Yan, X. Dip-coating for fibrous materials: mechanism, methods and applications. *Journal of Sol-Gel Science and Technology* **2017**, *81*, 378–404.

(19) Schuster, W. R.; Pezzin, S. H.; Lafratta, F. H. Airbrushing of carbon nanotubes on glass fibers for electromagnetic shielding epoxy composites. *Polimeros* **2023**, *33*, e20230001.

(20) Mujika, F.; Vargas, G.; Ibarretxe, J.; De Gracia, J.; Arrese, A. Influence of the mod-

https://doi.org/10.26434/chemrxiv-2024-cl440 **ORCID:** https://orcid.org/0000-0002-4653-7570 Content not peer-reviewed by ChemRxiv. **License:** CC BY-NC-ND 4.0

ification with MWCNT on the interlaminar fracture properties of long carbon fiber composites. *Composites Part B: Engineering* **2012**, *43*, 1336–1340.

(21) Avila, A. F.; de Oliveira, A. M.; Leao, S. G.; Martins, M. G. Aramid fabric/nano-size dual phase shear thickening fluid composites response to ballistic impact. *Composites Part A: Applied Science and Manufacturing* **2018**, *112*, 468–474.

(22) Carmignato, S.; Dewulf, W.; Leach, R. *Industrial X-ray computed tomography*; Springer, 2018; Vol. 10.

(23) Wang, Y.; Chen, Q.; Luo, Q.; Li, Q.; Sun, G. Characterizing damage evolution in fiber reinforced composites using in-situ X-ray computed tomography, deep machine learning and digital volume correlation (DVC). *Composites Science and Technology* **2024**, *254*, 110650.

(24) Upadhyay, S.; Smith, A. G.; Vandepitte, D.; Lomov, S. V.; Swolfs, Y.; Mehdikhani, M. Deep-learning versus greyscale segmentation of voids in X-ray computed tomography images of filament-wound composites. *Composites Part A: Applied Science and Manufacturing* **2024**, *177*, 107937.

(25) Galvez-Hernandez, P.; Smith, R.; Gaska, K.; Mavrogordato, M.; Sinclair, I.; Kratz, J. The effect of X-ray computed tomography scan parameters on porosity assessment of carbon fibre reinfored plastics laminates. *Journal of Composite Materials* **2023**, *57*, 4535–4548.

(26) Djukic, L. P.; Herszberg, I.; Walsh, W. R.; Schoeppner, G. A.; Prusty, B. G.; Kelly, D. W. Contrast enhancement in visualisation of woven composite tow architecture using a MicroCT Scanner. Part 1: Fabric coating and resin additives. *Composites Part A: Applied Science and Manufacturing* **2009**, *40*, 553–565.

(27) Ya, J.; Liu, Z.; Wang, Y. Micro-CT characterization on the meso-structure of three-

https://doi.org/10.26434/chemrxiv-2024-cl440 **ORCID:** https://orcid.org/0000-0002-4653-7570 Content not peer-reviewed by ChemRxiv. **License:** CC BY-NC-ND 4.0

dimensional full five-directional braided composite. *Applied Composite Materials* **2017**, *24*, 593–610.

(28) Pan, B.; Qian, K.; Xie, H.; Asundi, A. Two-dimensional digital image correlation for in-plane displacement and strain measurement: a review. *Measurement science and technology* **2009**, *20*, 062001.

(29) Pan, B. Digital image correlation for surface deformation measurement: historical developments, recent advances and future goals. *Measurement Science and Technology* **2018**, *29*, 082001.

(30) Dong, Y.; Pan, B. A review of speckle pattern fabrication and assessment for digital image correlation. *Experimental Mechanics* **2017**, *57*, 1161–1181.

(31) Bay, B. K.; Smith, T. S.; Fyhrie, D. P.; Saad, M. Digital volume correlation: three-dimensional strain mapping using X-ray tomography. *Experimental mechanics* **1999**, *39*, 217–226.

(32) Smith, T. S.; Bay, B. K.; Rashid, M. M. Digital volume correlation including rotational degrees of freedom during minimization. *Experimental Mechanics* **2002**, *42*, 272–278.

(33) Perie, J.-N.; Passieux, J.-C. *Advances in digital image correlation (DIC)*; MDPI, 2020.

(34) Gonzalez, J.; Lambros, J. A parametric study on the influence of internal speckle patterning for digital volume correlation in X-ray tomography applications. *Experimental Techniques* **2016**, *40*, 1447–1459.

(35) Borstnar, G.; Gillard, F.; Mavrogordato, M.; Sinclair, I.; Spearing, S. Three-dimensional deformation mapping of Mode I interlaminar crack extension in particle-toughened interlayers. *Acta Materialia* **2016**, *103*, 63–70.

(36) Bay, B. K. Methods and applications of digital volume correlation. *The Journal of Strain Analysis for Engineering Design* **2008**, *43*, 745–760.

https://doi.org/10.26434/chemrxiv-2024-cl440 **ORCID:** https://orcid.org/0000-0002-4653-7570 Content not peer-reviewed by ChemRxiv. **License:** CC BY-NC-ND 4.0

(37) Becker, T. H. Extracting fracture properties from digital image and volume correlation displacement data: A review. *Strain* **2023**,

(38) Lecomte-Grosbras, P.; Rethore, J.; Limodin, N.; Witz, J.-F.; Brieu, M. Three-dimensional investigation of free-edge effects in laminate composites using x-ray tomography and digital volume correlation. *Experimental Mechanics* **2015**, *55*, 301–311.

(39) Vrgovc, A.; Tomivcevic, Z.; Smaniotto, B.; Hild, F. Characterization of glass fiber reinforced polymer via digital volume correlation: Quantification of strain activity and damage growth. *Composites Science and Technology* **2023**, *234*, 109932.

(40) Mehdikhani, M.; Breite, C.; Swolfs, Y.; Soete, J.; Wevers, M.; Lomov, S. V.; Gorbatikh, L. Digital volume correlation for meso/micro in-situ damage analysis in carbon fiber reinforced composites. *Composites Science and Technology* **2021**, *213*, 108944.

(41) Schoberl, E.; Mavrogordato, M.; Sinclair, I.; Spearing, S. Fibre direction strain measurement in a composite ply under pure bending using Digital Volume Correlation and Micro-focus Computed Tomography. *Journal of Composite Materials* **2020**, *54*, 1889–1912.

(42) Srisuriyachot, J.; Benezech, J.; Couegnat, G.; McNair, S. A.; Maierhofer, T.; Butler, R.; Lunt, A. J. Synchrotron micro-CT in kink-band formation of UD-CFRP laminates with microdefects. *Composites Part B: Engineering* **2023**, *266*, 111038.

(43) Brault, R.; Germaneau, A.; Dupre, J.-C.; Doumalin, P.; Mistou, S.; Fazzini, M. In-situ analysis of laminated composite materials by X-ray micro-computed tomography and digital volume correlation. *Experimental Mechanics* **2013**, *53*, 1143–1151.

(44) Goossens, E.; Aalling-Frederiksen, O.; Tack, P.; Van den Eynden, D.; Walsh-Korb, Z.; Jensen, K. M.; De Buysser, K.; De Roo, J. From Gel to Crystal: Mechanism of HfO2 and ZrO2 Nanocrystal Synthesis in Benzyl Alcohol. *Journal of the American Chemical Society* **2024**, *146*, 10723–10734.

https://doi.org/10.26434/chemrxiv-2024-cl440 **ORCID:** https://orcid.org/0000-0002-4653-7570 Content not peer-reviewed by ChemRxiv. **License:** CC BY-NC-ND 4.0

(45) Hens, Z.; Martins, J. C. A solution NMR toolbox for characterizing the surface chemistry of colloidal nanocrystals. *Chemistry of Materials* **2013**, *25*, 1211–1221.

(46) De Roo, J.; Yazdani, N.; Drijvers, E.; Lauria, A.; Maes, J.; Owen, J. S.; Van Driessche, I.; Niederberger, M.; Wood, V.; Martins, J. C., et al. Probing solvent–ligand interactions in colloidal nanocrystals by the NMR line broadening. *Chemistry of Materials* **2018**, *30*, 5485–5492.

(47) Gomes, R.; Hassinen, A.; Szczygiel, A.; Zhao, Q.; Vantomme, A.; Martins, J. C.; Hens, Z. Binding of phosphonic acids to CdSe quantum dots: A solution NMR study. *The Journal of Physical Chemistry Letters* **2011**, *2*, 145–152.

(48) Karapappas, P.; Tsantzalis, S.; Fiamegou, E.; Vavouliotis, A.; Dassios, K.; Kostopoulos, V. Multi-wall carbon nanotubes chemically grafted and physically adsorpted on reinforcing carbon fibres. *Advanced Composites Letters* **2008**, *17*.

(49) He, Y.; Sai, L.-M.; Lu, H.-T.; Hu, M.; Lai, W.-Y.; Fan, Q.-L.; Wang, L.-H.; Huang, W. Microwave-assisted synthesis of water-dispersed CdTe nanocrystals with high luminescent efficiency and narrow size distribution. *Chemistry of Materials* **2007**, *19*, 359–365.

(50) Williams, D. B. G.; Lawton, M. Drying of organic solvents: quantitative evaluation of the efficiency of several desiccants. *The Journal of organic chemistry* **2010**, *75*, 8351–8354.

(51) Masschaele, B.; Dierick, M.; Van Loo, D.; Boone, M. N.; Brabant, L.; Pauwels, E.; Cnudde, V.; Van Hoorebeke, L. HECTOR: A 240kV micro-CT setup optimized for research. Journal of Physics: Conference Series. 2013; p 012012.

https://doi.org/10.26434/chemrxiv-2024-cl440 **ORCID:** https://orcid.org/0000-0002-4653-7570 Content not peer-reviewed by ChemRxiv. **License:** CC BY-NC-ND 4.0

TOC Graphic

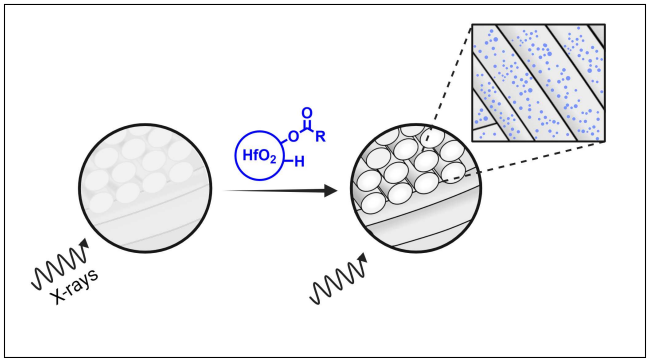

https://doi.org/10.26434/chemrxiv-2024-cl440 **ORCID:** https://orcid.org/0000-0002-4653-7570 Content not peer-reviewed by ChemRxiv. **License:** CC BY-NC-ND 4.0